Magnetic frustration in (LaA)CoNbO6 (A=Ca, Sr, and Ba) double perovskites

Magnetic frustration in $(LaA)CoNbO_6$ (A=Ca, Sr, and Ba) double perovskites

Jan-Willem G. Bos
Department of Chemistry, University of Cambridge, Lensfield Road, Cambridge, CB2 1EW, United Kingdom

J. Paul Attfield
Centre for Science at Extreme Conditions, University of Edinburgh, West Mains Road, Edinburgh, EH9 3JJ, United Kingdom

(Received 15 June 2004; revised manuscript received 7 September 2004; published 17 November 2004)

The crystal and magnetic structures of the $(LaA)CoNbO_6$ (A=Ca, Sr, and Ba) double perovskites have been investigated. The A=Ca and Sr compounds crystallize with a monoclinic $P2_1/n$ superstructure while the larger A=Ba gives a tetragonal $I4/m$ superstructure. These materials have a rocksalt ordered arrangement of Co and Nb with almost no inversion (<1%) for A=Ca and 4% inversion for A=Sr and Ba. Magnetic susceptibility measurements reveal antiferromagnetic ordering transitions with Neel temperatures of 17 K (A=Ca), 16 K (A=Sr), and 10 K (A=Ba). The low temperature antiferromagnetic ordering is described by the magnetic propagation vector $\mathbf{k}=(\frac{1}{2}\ 0\ \frac{1}{2})$ for all materials. The saturated cobalt magnetic moment decreases from 2.97(2) μ_B to 2.52(3) μ_B to 1.85(5) μ_B for A=Ca, Sr, and Ba, respectively. The decrease of ordering temperature and moment with increasing size of A evidences magnetic frustration due to competition between 90° superexchange pathways. This is shown to be a general feature in antiferromagnetic double perovskites.

DOI: 10.1103/PhysRevB.70.174434 PACS number(s): 75.30.−m, 75.25.+z, 61.12.Ld, 61.66.Fn

I. INTRODUCTION

The interplay of magnetism and electronic transport in double perovskite oxides[1] has been of recent interest following the discovery of itinerant ferrimagnetism and low field magnetoresistance in Sr_2FeMoO_6 and Sr_2FeReO_6 (Refs. 2 and 3). The itinerancy and ferrimagnetism arise from a double exchange type mechanism in which ordering and electronic configurations of the transition metal cations play a critical role.[4] Structurally, the 3d (B) and 4d or 5d (B') transition metal cations are ordered in an alternating (rocksalt) manner within a perovskite lattice. Electronically, the 3d cation has a large spin (S=2 to 5/2 for Fe^{2+}-Fe^{3+}) whereas the 4d or 5d cation usually has $S \leqslant 1/2$. Equal spins of the 3d and 4 or 5d cations could result in a so-called half-metallic antiferromagnet (HMAF), where completely spin-polarized conduction occurs in a zero magnetization material.[5] Candidate HMAF double perovskite materials are, for example, $(LaA)CoRuO_6$ where both Co^{2+} and Ru^{5+} have S=3/2. However, previous studies showed these materials are antiferromagnetic with two opposed Co and two opposed Ru spin sublattices. They are variable range hopping semiconductors, with T_N=96 K for A=Ca and 85 K for A=Sr, and show no magnetotransport effects.[6,7] In fact, the majority of nonmetallic double perovskites are antiferromagnetic although Sr_2CaReO_6 and Sr_2MgReO_6, where Re-Re exchange interactions are geometrically frustrated, behave as spin-glasses.[8,9]

Here, we report a study into the crystal and magnetic structures of the $(LaA)CoNbO_6$ (A=Ca, Sr, and Ba) double perovskites. $LaSrCoNbO_6$ was previously reported to be cubic with a=7.99 Å (Ref. 10); the Ca and Ba materials have not been reported. In addition, we present a comparison of the magnetic propagation vectors reported for antiferromagnetic Mn, Fe, and Co double perovskites. We show that magnetic frustration is significant in B-cation ordered antiferromagnetic double perovskites and analyze its origins.

II. EXPERIMENT

$(LaA)CoNbO_6$ (A=Ca, Sr, and Ba) were prepared as yellow-brown polycrystalline powders by solid state reaction. Stoichometric amounts of high purity La_2O_3, ACO_3 (A=Ca, Sr, Ba), Co_3O_4 and Nb_2O_5 were ground, pressed into pellets and treated for 2 h at 900 °C. The resulting powders were reground, repressed and heated for 48 h (with three intermediate regrinding steps) at 1300 °C for A=Ca, Sr and at 1350 °C for A=Ba. X-ray powder diffraction (XPD) on a Philips PW1710 or Bruker D8 diffractometer showed the Ca and Sr materials to be phase pure. A small $LaNbO_4$ impurity (~1 mass %) was found for $LaBaCoNbO_6$.

The crystal and magnetic structures of the title materials have been investigated using neutron powder diffraction (NPD). NPD experiments on $LaCaCoNbO_6$ and $LaSrCoNbO_6$ were performed on the high resolution D2B diffractometer at the Institute Laue Langevin (ILL) in

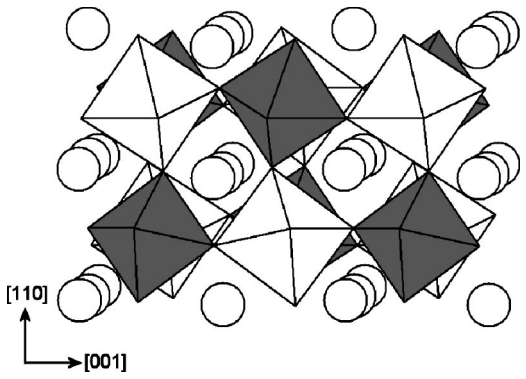

FIG. 1. View of the structure of monoclinic $LaCaCoNbO_6$ at RT. Shaded/unshaded polyhedra are occupied by Nb/Co.

TABLE I. Lattice constants, refined atomic parameters and residuals for (La*A*)$CoNbO_6$ (*A*=Ca, Sr) at RT and 4 K, and at 4 K for *A*=Ba.[a]

	$LaCaCoNbO_6$		$LaSrCoNbO_6$		$LaBaCoNbO_6$
	RT	4 K	RT	4 K	4 K
a (Å)	5.5509(1)	5.53934(8)	5.6423(3)	5.6331(3)	5.6902(6)
b (Å)	5.65552(9)	5.65676(7)	5.6506(3)	5.6465(3)	
c (Å)	7.8909(1)	7.8733(1)	7.9693(4)	7.9573(4)	8.060(2)
β (deg)	89.860(2)	89.826(2)	89.799(5)	89.819(5)	
Volume ($Å^3$)	247.724(8)	246.707(4)	254.08(2)	253.100(8)	260.97(1)
La/*A* *x*	0.0088(4)	0.0095(3)	0.004(1)	0.0054(8)	
y	0.0438(2)	0.0456(2)	0.0246(5)	0.0291(3)	
z	0.2512(4)	0.2520(3)	0.252(1)	0.2520(9)	
$100\times U$ ($Å^2$)	1.11(3)	0.54(3)	1.37(7)	0.67(6)	0.4(1)
Co/Nb occ	0.992(7)/0.008(7)		0.96(1)/0.04(1)		0.96(2)/0.04(2)
$100\times U$ ($Å^2$)	0.77(4)	0.49(4)	0.85(7)	0.41(7)	0.2(1)
Nb/Co occ	0.992(7)/0.008(7)		0.96(1)/0.04(1)		0.96(2)/0.04(2)
$100\times U$ ($Å^2$)	0.77(4)	0.49(4)	0.85(7)	0.41(7)	0.2(1)
O1 *x*	0.2875(5)	0.2868(4)	0.281(1)	0.278(1)	0.044(6)
y	0.3019(5)	0.3026(4)	0.292(1)	0.294(1)	0
z	0.0444(4)	0.0445(3)	0.0363(9)	0.0352(8)	0.256(5)
$100\times U$ ($Å^2$)	1.09(7)	0.65(6)	1.6(2)	1.1(2)	0.5(2)
O2 *x*	0.1977(4)	0.1964(4)	0.211(1)	0.211(1)	0.227(3)
y	−0.2141(5)	−0.2140(4)	−0.228(1)	−0.225(1)	0.293(2)
z	0.0466(3)	0.0488(3)	0.0340(9)	0.0406(8)	0.026(2)
$100\times U$ ($Å^2$)	1.03(7)	0.51(6)	1.9(2)	1.0(2)	0.5(2)
O3 *x*	−0.0857(3)	−0.0873(3)	−0.065(1)	−0.068(1)	
y	0.4746(3)	0.4732(3)	0.4885(7)	0.4867(6)	
z	0.2419(4)	0.2427(3)	0.245(1)	0.2451(9)	
$100\times U$ ($Å^2$)	1.07(4)	0.69(4)	0.9(1)	0.69(9)	
χ^2	2.41	2.38	3.75	3.47	3.04
wR_p	4.45%	4.20%	5.89%	5.28%	1.80%
R_p	3.48%	3.21%	4.65%	4.14%	1.14%
R_F^2	2.84%	3.26%	4.57%	5.81%	12.31%

[a](La*A*)$CoNbO_6$ (*A*=Ca, Sr): Space group $P2_1/n$, La/*A*, O1, O2, O3 at 4*e* (x,y,z), Nb/Co at 2*c* $(\frac{1}{2},0,\frac{1}{2})$, Co/Nb at 2*d* $(\frac{1}{2},0,0)$. (*A*=Ba): Space group $I4/m$, La/Ba at 4*d* $(0,\frac{1}{2},\frac{1}{4})$, Nb/Co at 2*b* $(0,0,\frac{1}{2})$ and Co/Nb at 2*a* (0,0,0), O1 at 4*e* $(0,0,z)$ occupancy: 0.25 and O2 at 8*h* $(x,y,0)$ occupancy: 0.5.

Grenoble, France. Data were collected in the $8\leqslant 2\theta\leqslant 160°$ range in 0.05° increments at room temperature (RT) and 4 K. The neutron wavelength was 1.5943 Å. For $LaBaCoNbO_6$, NPD data were collected at 4 K using the D20 instrument. The instrument was in the high-flux setting (monochromator takeoff angle 42°) with a wavelength of 2.4156 Å. Data were collected in the $10\leqslant 2\theta\leqslant 140°$ range with 0.1° increments.

The GSAS suite of programs[11] was used for Rietveld fitting of the NPD and XPD data. A Pseudo-Voigt function convoluted with an axial divergence contribution was used to describe the peak shape for both types of data.

The dc magnetic susceptibility was measured using a Quantum Design MPMS magnetometer. Zero field cooled (ZFC) and field cooled (FC) data (H=500 Oe) were collected in the $5\leqslant T\leqslant 300$ K range.

III. RESULTS

A. Crystal structures

1. $LaCaCoNbO_6$ and $LaSrCoNbO_6$

Rietveld analysis of the NPD data showed (La*A*)$CoNbO_6$ (*A*=Ca, Sr) to crystallize with the monoclinic $P2_1/n$ superstructure commonly observed for double perovskites. The $P2_1/n$ superstructure allows for 1:1 *B*-cation ordering and describes the $b^-b^-c^+$ system of three octahedral tilts in the Glazer notation, as discussed below. Rietveld analysis showed Co and Nb to be almost fully ordered for *A*=Ca (<1% inversion) and with 4% inversion for *A*=Sr. The crystal structure for *A*=Ca is illustrated in Fig. 1. The lattice constants and refined atomic parameters at RT and 4 K are given in Table I. Selected bond lengths and bond angles at

TABLE II. Selected bond lengths (Å), bond angles (deg) and bond valence sums (BVS) for (LaA)CoNbO$_6$ (A=Ca, Sr and Ba).

	LaCaCoNbO$_6$		LaSrCoNbO$_6$		LaBaCoNbO$_6$
	RT	4 K	RT	4 K	4 K
⟨La/A—O⟩	2.572(3)	2.564(2)	2.698(7)	2.691(6)	2.852(3)
Nb—O1	1.982(3)	1.974(2)	1.996(7)	1.976(6)	1.96(4) (2x)
Nb—O2	1.989(2)	1.987(2)	1.969(8)	1.983(6)	1.95(2) (4x)
Nb—O3	1.971(3)	1.975(2)	1.985(8)	1.987(7)	
⟨Nb—O⟩	1.981(2)	1.979(1)	1.983(4)	1.982(6)	1.95(2)
Co—O1	2.104(3)	2.108(2)	2.081(7)	2.094(6)	2.07(4) (2x)
Co—O2	2.101(2)	2.107(2)	2.100(7)	2.089(5)	2.12(2) (4x)
Co—O3	2.098(3)	2.090(2)	2.069(8)	2.065(8)	
⟨Co—O⟩	2.101(2)	2.102(1)	2.083(4)	2.083(6)	2.10(2)
Co—O1—Nb	151.7(2)	151.7(1)	157.2(3)	156.9(4)	180
Co—O2—Nb	151.3(2)	150.4(1)	157.6(3)	156.8(3)	163.8(2)
Co—O3—Nb	151.7(1)	151.1(1)	158.7(3)	158.1(3)	
⟨Co—O—Nb⟩	151.6(1)	151.1(1)	157.8(2)	157.3(3)	169.2(2)
BVS La	2.96(1)		2.78(2)		2.1(1)
A	1.73(1)		2.25(2)		2.9(1)
Co	1.99(1)		2.08(2)		2.0(1)
Nb	4.97(2)		4.94(4)		5.5(2)
O1	1.94(1)		1.95(2)		2.0(1)
O2	1.91(1)		1.95(2)		2.1(1)
O3	1.99(1)		1.95(2)		

RT and 4 K, and bond valence sums (BVS) at RT are given in Table II. The BVS were calculated using the VALIST program[12] and indicate the presence of Co^{2+} ($3d^7$) and Nb^{5+} ($4d^0$) for both materials. This is in agreement with the observation by Anderson *et al.* in their review of double perovskites[1] that charge differences $\geqslant 3$ are generally required to obtain high degrees of charge ordering. The mean Co—O and Nb—O bond lengths are identical at 4 K and RT, while the La/A—O bond lengths and Co—O—Nb bond angles increase slightly.

In Glazer notation,[13,14] a tilt system is described by specifying the rotations of the BO_6 octahedra about each of the three Cartesian axes. The rotations about each axis are described by two parameters. The first is a letter specifying the magnitude of the rotation around that axis, relative to the magnitude of the other rotations around the Cartesian axes. The second parameter is a superscript indicating whether rotations in adjacent layers are in the same direction or opposite. The tilting associated with the $P2_1/n$ space group is $b^-b^-c^+$ (where the rotations around the x and y axes have the same magnitude). The tilting angle of the $(Co/Nb)O_6$ octahedra can be defined as $(180-\phi)/2$, where ϕ is the Co—O—Nb bond angle (ϕ=180° for a cubic perovskite). From Table II, tilting angles of 14.2(2), 14.4(2), and 14.2(1) for A=Ca, and 11.4(3), 11.2(3), and 10.7(3) for A=Sr are found at RT.

2. LaBaCoNbO$_6$

Analysis of RT x-ray data and low temperature NPD data showed LaBaCoNbO$_6$ to crystallize with the $I4/m$ superstructure. This superstructure can accommodate 1:1 B-cation ordering and corresponds to the $a^0a^0c^-$ Glazer one tilt system. The crystal structure of LaBaCoNbO$_6$ at 4 K is illustrated in Fig. 2(a). Rietveld analysis of x-ray and NPD data showed Co and Nb to be ordered over the B-sites with 4% inversion. The refined atomic parameters and lattice constants at 4 K are given in Table I. Initial Rietveld fits to the NPD data showed anomalously large values for the oxygen temperature factors. This was addressed by splitting the oxygen sites [see Table I, and as illustrated in Fig. 2(b)], thereby allowing for disordered octahedral tilts. Selected bond lengths, bond angles and BVS for LaBaCoNbO$_6$ at 4 K are given in Table II. The BVS indicate the presence of Co^{2+} ($3d^7$) and Nb^{5+} ($4d^0$) oxidation states as observed for the A=Ca and Sr analogs. The average Co—O and Nb—O bond lengths are found to vary little with temperature or with A (Table II) in (LaA)CoNbO$_6$ indicating the "rigidity" of these bonds. The ordered octahedral tilt angle as calculated from the Co—O2—Nb bond angle is $8.1(2)^0$, and the disordered tilts are $7.2(2)^0$ around the x,y-axes and $9.5(6)^0$ around the z-axis. This shows that the local disordered tilts are of comparable magnitude to the long-range ordered one. Hence, the transition from the $a^0a^0c^-$ one-tilt structure of LaBaCoNbO$_6$ to the $b^-b^-c^+$ three tilt system for smaller A=Sr, Ca is mainly a disorder-to-order transition rather than a displacive change. The larger Ba cation stabilizes the $a^0a^0c^-$ one-tilt system whereas the smaller Ca and Sr cations favor the $b^-b^-c^+$ three-tilt system.

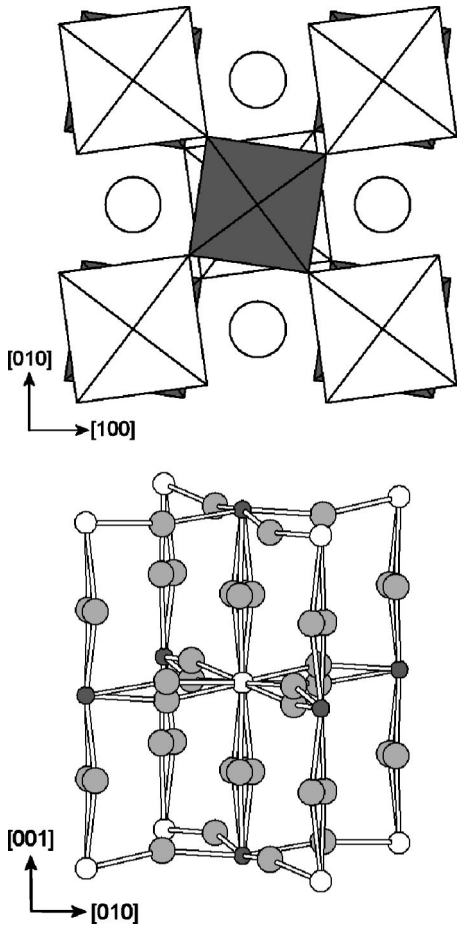

FIG. 2. Views of the structure of tetragonal $LaBaCoNbO_6$. (a) Idealized polyhedral view illustrating the $a^0a^0c^-$ tilt system. Shaded/unshaded polyhedra are occupied by Nb/Co. (b) Showing the disordered tilts in the refinement model.

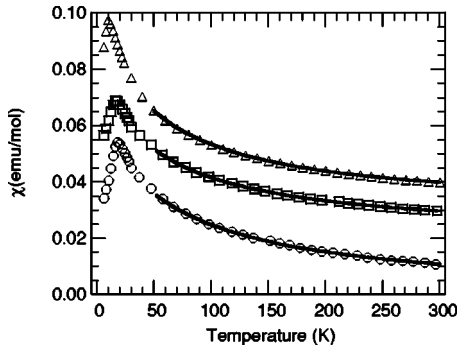

FIG. 3. Zero field cooled magnetic susceptibilities for $LaCaCoNbO_6$ (circles), $LaSrCoNbO_6$ (squares, offset by 0.02 emu/mol), and $LaBaCoNbO_6$ (triangles, offset by 0.03 emu/mol). Curie-Weiss fits are shown.

B. Magnetization

Magnetic susceptibility measurements revealed three-dimensional antiferromagnetic ordering transitions for all $(LaA)CoNbO_6$ materials (Fig. 3) at low temperatures. Neel temperatures (T_N) of 17 K (A=Ca), 16 K (A=Sr), and 10 K (A=Ba) were found. The ZFC and FC susceptibilities coincide in the 5–300 K temperature range confirming the presence of antiferromagnetic and paramagnetic states without magnetic impurities. Paramagnetic moments (μ_{eff}) and Weiss temperatures (θ) were determined by Curie-Weiss fits to the susceptibility data in the $50<T<300$ K range. The Weiss temperatures (Table III) are all negative and the effective magnetic moment decreases slightly from 5.6 μ_B/f.u. for A=Ca to 5.3 μ_B/f.u. for A=Sr and Ba. The experimental values are substantially higher than the expected spin-only value for high-spin Co^{2+} ($S=3/2$) $\mu_{\text{eff}}=3.9$ μ_B/f.u., indicating an orbital momentum contribution to the paramagnetic

TABLE III. Neel temperatures, Curie-Weiss parameters, frustration factors (f), magnetic representations, basis vectors, magnetic saturation moments at 4 K, angle $\phi_{\text{Co1,Co4}}$ between moments on Co1 and Co4, and reduced χ^2 for $(LaA)CoNbO_6$ (A=Ca, Sr and Ba). [Co1 and Co4 are related by the $(\frac{1}{2}\ \frac{1}{2}\ \frac{1}{2})$ translation operation and correspond to atoms 1 and 4 in Fig. 5.]

	A=Ca				A=Sr				A=Ba
T_N (K)	17				16				10
μ_{eff}(μ_B/f.u.)	5.65(3)				5.30(2)				5.25(2)
θ (K)	−61(1)				−63(1)				−48(1)
f	3.6				3.9				4.8
Γ_{Mag}	$3\Gamma_2$	$3\Gamma_4$	parallel	antiparallel	$3\Gamma_2$	$3\Gamma_4$	parallel	antiparallel	$3\Gamma_1$
Basis vectors: Co1	[111]	[111]	[111]	[111]	[111]	[111]	[111]	[111]	[111]
Basis vectors: Co4	$[\bar{1}\bar{1}\bar{1}]$	$[\bar{1}1\bar{1}]$	[111]	$[\bar{1}\bar{1}\bar{1}]$	$[\bar{1}\bar{1}\bar{1}]$	$[\bar{1}1\bar{1}]$	[111]	$[\bar{1}\bar{1}\bar{1}]$	[111]
μ_x (μ_B)	0.02(6)	0.03(6)	−0.05(7)	−0.04(8)	0	0	0	0	0.24(8)
μ_y (μ_B)	−1.97(7)	−1.97(8)	−1.97(8)	−2.10(8)	1.7(1)	1.8(1)	1.7(1)	1.8(1)	0
μ_z (μ_B)	2.22(6)	−2.21(7)	−2.21(7)	2.07(8)	−1.9(1)	1.8(1)	−1.9(1)	−1.7(1)	1.83(4)
μ_{Co} (μ_B)	2.97(2)	2.96(2)	2.97(2)	2.95(2)	2.52(3)	2.52(3)	2.52(3)	2.52(2)	1.85(5)
$\phi_{\text{Co1,Co4}}$ (deg)	97(1)	83(1)	0	180	113(8)	87(8)	0	180	0
χ^2	2.38	2.39	2.43	2.42	3.48	3.47	3.50	3.48	3.04

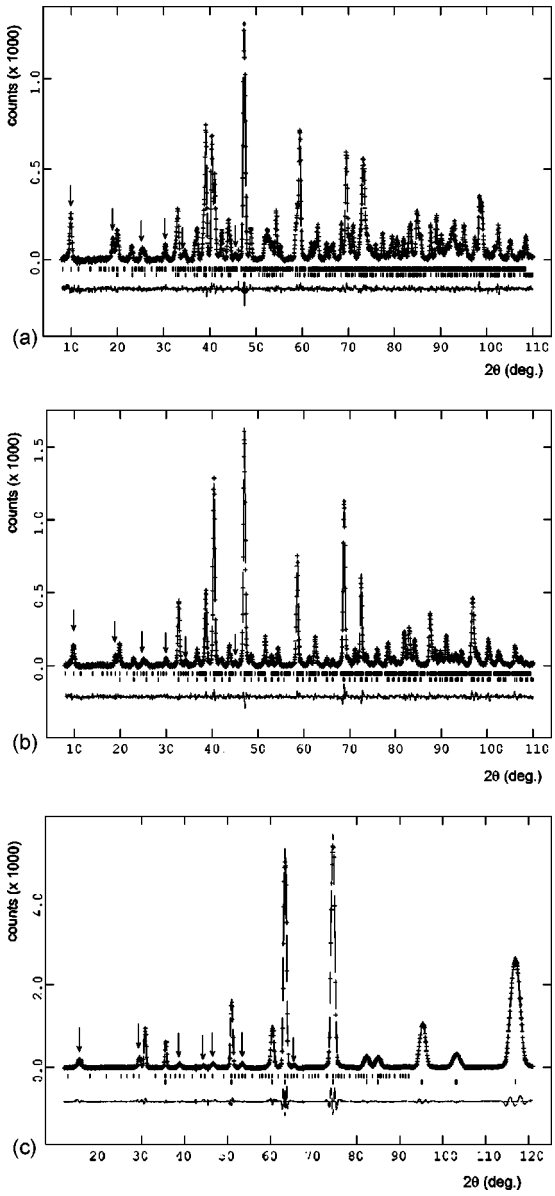

FIG. 4. Observed (crosses), calculated (full line), and difference NPD Rietveld profiles for (a) LaCaCoNbO$_6$, (b) LaSrCoNbO$_6$, and (c) LaBaCoNbO$_6$ at 4 K. Reflection markers correspond to the Bragg positions of the structural (top) and magnetic phase (bottom). Prominent magnetic superstructure peaks are arrowed.

moment. High-spin octahedral Co^{2+} has a $^4T_{1g}$ ground state and spin-orbit coupling typically leads to moments of $\sim 5.2\ \mu_B$ (Ref. 15).

C. Magnetic structures

Magnetic diffraction peaks were observed in the 4 K NPD patterns for all materials (Fig. 4). These were indexed by the propagation vector $(\frac{1}{2}\ 0\ \frac{1}{2})$, showing that an antiferromagnetic Co sublattice is present. [Due to the tetragonal cell symmetry, the magnetic reflections for A=Ba can equivalently be indexed by the $(0\ \frac{1}{2}\ \frac{1}{2})$ propagation vector, but this is not true for monoclinic A=Ca and Sr.] Representational analysis was used to obtain symmetry allowed models for the magnetic structures, which have been refined using reverse Monte Carlo (RMC) simulations and Rietveld least squares fitting. Representational analysis allows the determination of the symmetry allowed magnetic structures that can result from a second-order magnetic phase transition, given the crystal structure above the transition and the propagation vector of the magnetic ordering. These calculations were carried out using version 2 K of the program Sara*h*-Representational Analysis[16] and closely follow the method of Munoz *et al.*[17] They involve first the determination of the space group symmetry elements, g, that leave the propagation vector $\mathbf{k}$ invariant: these form the small group $G_\mathbf{k}$. The magnetic representation of a crystallographic site can then be decomposed in terms of the irreducible representations (IRs) of the small group $G_\mathbf{k}$:

$$\Gamma_{\mathrm{Mag}} = \sum_\nu n_\nu \Gamma_\nu^\mu,$$

where n_ν is the number of times that the IR Γ_ν appears in the magnetic representation Γ_{mag} for the chosen crystallographic site. For the A=Ca and Sr materials, the small group $G_\mathbf{k}$ coincides with the $P2_1/n$ space group, whereas for A=Ba ($I4/m$) only $g_1=\{E|0\ 0\ 0\}$ and $g_5=\{I|0\ 0\ 0\}$ leave $\mathbf{k}$ invariant or transform it to an equivalent vector. The decomposition of the magnetic representation (in terms of the nonzero IRs of $G_\mathbf{k}$) for the Co sites in the A=Ca, Sr, and Ba materials, and their associated basis vectors are given in Table III. For the $P2_1/n$ materials (A=Ca,Sr), Co atoms related by the $(\frac{1}{2}\ \frac{1}{2}\ \frac{1}{2})$ translation vector can have their magnetic moments arranged in two possible ways, corresponding to $\Gamma_{\mathrm{mag}}=3\Gamma_2$ or $3\Gamma_4$. For the higher symmetry A=Ba ($I4/m$) material, the Co magnetic moments are arranged according to $\Gamma_{\mathrm{mag}}=3\Gamma_1$. Initially, the symmetry allowed models were refined using the Sara*h*-Refine program, which utilizes a RMC algorithm to perform a global search sampling all regions of phase space with an equal probability.[16] Approximately 250 RMC cycles were run for all allowed magnetic models. Following these simulations, the best solutions were Rietveld (least-squares) fitted to obtain the final solutions for the magnetic structures, which are given in Table III.

In addition, two other models describing collinear magnetic structures were considered for the monoclinic A=Ca and Sr materials. These models were obtained by considering a possible mixture of the basis vectors of the $3\Gamma_2$ and $3\Gamma_4$ representations.[17] The resulting basis vectors are given in Table III and they correspond to either a ferromagnetic coupling of the two Co moments in the unit cell or to an antiferromagnetic coupling. For A=Ca and Sr, the $3\Gamma_2$ and $3\Gamma_4$ representations and the two collinear models give almost identical fits to the magnetic diffraction. In all cases, μ_x is near zero and μ_y, μ_z have comparable magnitudes. (For A=Sr, μ_x was set to zero in the final refinement cycles to obtain more precise values of μ_y and μ_z.) The quality of the fit is identical for all magnetic models. For A=Ba, the magnetic moment is almost aligned along the c-axis with only a very small value for

TABLE IV. Average *A*-cation radii (Shannon, Ref. 19), lattice constants at 300 K (RT), Neel temperatures, frustration factors (f), and magnetic propagation vectors **k** for a variety of monoclinic cation ordered double perovskites.

	Ref.	$\langle r_A \rangle$ (Å)	a (Å)	b (Å)	c (Å)	β (deg)	T_N (K)	f	**k**
Ca_2MnWO_6	17	1.180	5.4694(2)	5.6504(2)	7.8122(3)	90.179(3)	17	3.6	$(0\ \frac{1}{2}\ \frac{1}{2})$
$LaCaMnNbO_6$	20	1.198	5.5929(1)	5.7406(1)	7.9824(1)	89.897(1)	9	4.9	$(0\ \frac{1}{2}\ \frac{1}{2})$
$LaSrMnNbO_6$	21	1.263	5.6918(2)	5.7453(2)	8.0689(3)	90.043(6)	8	5.0	$(0\ \frac{1}{2}\ \frac{1}{2})$
Sr_2MnMoO_6	17	1.310	5.6671(1)	5.6537(1)	7.9969(2)	89.927(2)	15	7.2	$(\frac{1}{2}\ 0\ \frac{1}{2})$
Sr_2MnWO_6	17	1.310	5.6803(2)	5.6723(2)	8.0199(2)	89.936(3)	14	5.1	$(\frac{1}{2}\ 0\ \frac{1}{2})$
$LaBaMnNbO_6$	21	1.343	5.7713(1)		8.1687(3)		6.5	6.0	$(\frac{1}{2}\ 0\ \frac{1}{2})$[a]
Ba_2MnMoO_6	22	1.470	8.1680(2)				11	8.5	$(\frac{1}{2}\ \frac{1}{2}\ \frac{1}{2})$
Ba_2MnWO_6	23	1.470	8.1985(2)				9	7.2	$(\frac{1}{2}\ \frac{1}{2}\ \frac{1}{2})$
$LaSrFeNbO_6$	21	1.263	5.6707(2)	5.6665(2)	8.0006(3)	89.960(6)	23	4.8	$(\frac{1}{2}\ 0\ \frac{1}{2})$
Sr_2FeWO_6	24 and 25	1.310	5.6480(4)	5.6088(4)	7.9362(6)	89.99(2)	37	0.6	$(0\ \frac{1}{2}\ \frac{1}{2})$
$LaCaCoNbO_6$		1.198	5.5509(1)	5.6555(1)	7.8909(1)	89.860(2)	17	3.6	$(\frac{1}{2}\ 0\ \frac{1}{2})$
$LaCaCoRuO_6$	6	1.198	5.4977(1)	5.5687(1)	7.7939(2)	90.013(8)	96	2.0	$(\frac{1}{2}\ 0\ \frac{1}{2})$
La_2CoRuO_6	21	1.216	5.5711(1)	5.6289(1)	7.8813(2)	89.986(9)	25	3.5	$(\frac{1}{2}\ 0\ \frac{1}{2})$
$LaSrCoNbO_6$		1.263	5.6423(3)	5.6500(2)	7.9684(3)	89.805(5)	16	3.9	$(\frac{1}{2}\ 0\ \frac{1}{2})$
$LaSrCoRuO_6$	7	1.263	5.5890(1)	5.5623(2)	7.8743(2)	89.960(7)	85	0.2	$(\frac{1}{2}0\ \frac{1}{2})$
Sr_2CoWO_6	15	1.310	5.6123(1)	5.5875(1)	7.8994(1)	90.041(3)	24	2.6	$(\frac{1}{2}\ 0\ \frac{1}{2})$
$LaBaCoNbO_6$		1.343	5.7098(1)		8.0655(3)		10	4.8	$(\frac{1}{2}\ 0\ \frac{1}{2})$[a]

[a]$k=(\frac{1}{2}\ 0\ \frac{1}{2})$ and $(0\ \frac{1}{2}\ \frac{1}{2})$ are equivalent for a tetragonal cell.

μ_x. The resultant magnetic moment decreases from $2.97(2)\mu_B$ (A=Ca) to $2.52(3)\mu_B$ (A=Sr) to $1.85(5)\mu_B$ (A=Ba). The expected spin-only saturation moment for high-spin Co^{2+} is 3 μ_B.

IV. MAGNETIC FRUSTRATION

An overview of the lattice constants, magnetic ordering temperatures, frustration factors ($f=|\theta|/T_N$) (Ref. 18) and magnetic propagation vectors for a large number of antiferromagnetic double perovskites including the title materials is given in Table IV. Two trends are evident, a *decrease* in T_N with increasing average *A*-cation size ($\langle r_A \rangle$) for any combination of *B*-cations, although an *increase* is usually expected as tilt angles decrease with increasing $\langle r_A \rangle$, and an accompanying increase in the magnetic frustration factor f (f is typically <3 for unfrustrated cubic antiferromagnets and >10 for significantly frustrated materials).[18] The current values for f are intermediate but the magnetic frustration is nevertheless significant since it has measurable effects on the Neel temperatures and saturation moments.

Magnetic frustration arises when a large fraction of the magnetic sites in a lattice are subject to competing or contradictorary constraints. When frustration arises purely from the geometry or topology of the lattice it is termed geometric frustration. The canonical example is any lattice based on an equilateral triangle, such as the Kagome lattice. In three dimensions, the antiferromagnetic face centered cubic (fcc) and pyrochlore lattices are geometrically frustrated. The former is based on edge-shared tetrahedra, and the latter on corner-shared tetrahedra of interactions. As discussed above, double perovskites have a rocksalt ordered *B*-cation sublattice. The rocksalt sublattice consists of interpenetrating *B* and *B′* fcc sublattices, giving rise to magnetic frustration. A suppression of magnetic order is already known in the Sr_2BReO_6 (B=Mg,Ca) double perovskites due to the geometrically frustrated Re-Re exchange interactions.[8,9] Most other insulating double perovskites, such as (La*A*)$CoNbO_6$ (A=Ca, Sr, and Ba) show long range antiferromagnetic order and at first sight do not appear to be magnetically frustrated. However, the decrease in T_N and ordered moment μ_{Co} and the increase in f for (La*A*)$CoNbO_6$ (A=Ca, Sr, and Ba) with increasing $\langle r_A \rangle$ (Table III), and similar trends in other double perovskites (Table IV), are explained from the frustrated 90° interactions in the fcc Co-sublattice.

Part of the fcc Co-sublattice for $LaCaCoNbO_6$ is depicted in Fig. 5. Atoms 1–4 each define a primitive cubic sublattice, in which Co spins are connected by 180° Co—O—Nb—O—Co bridges (180° refers to the central O—Nb—O angle in an undistorted cubic double perovskite). The antiferromagnetic J_{180} superexchange interactions in each sublattice are fully satisfied. The interactions between the four magnetic sublattices (1–4) are via 90° Co—O—Nb—O—Co exchange pathways. In a cubic fcc lattice, one J_{180} and one J_{90} exchange interaction are present. For the monoclinic double perovskite case, there are two J_{180} and four J_{90} interactions, as illustrated in Fig. 5(b). The inequivalence of the J_{90} interactions determines the magnetic arrangement. The relative directions of the moments in the $3\Gamma_2$ or $3\Gamma_4$ solutions (Table III) are consistent with the relative strengths

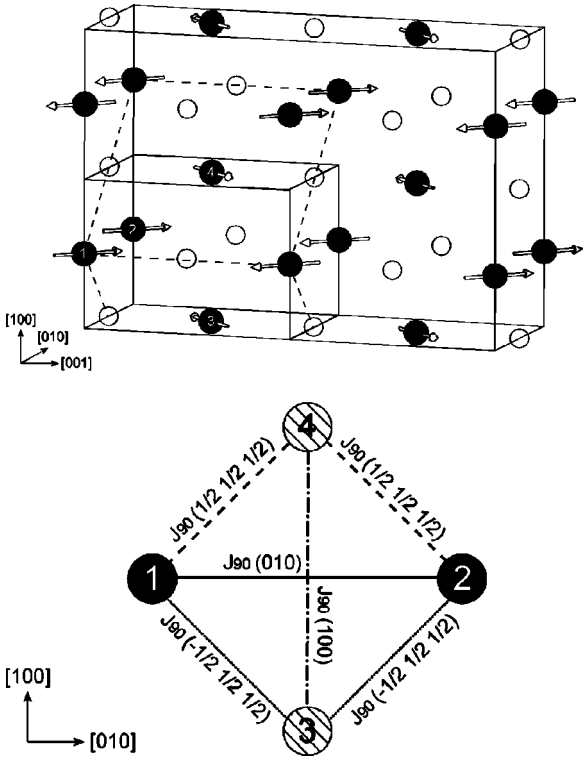

FIG. 5. (a) Relative orientations of the crystallographic, and magnetic cells and the underlying Co-fcc cell (broken line) for $LaCaCoNbO_6$, the spin directions shown are for the $3\Gamma_2$ solution. (b) The topology of 90° Co—O—Nb—O—Co superexchange interactions between the four Co sublattices.

$J_{90}(100) > J_{90}(\frac{1}{2}\ \frac{1}{2}\ \frac{1}{2}) \approx J_{90}(-\frac{1}{2}\ \frac{1}{2}\ \frac{1}{2}) > J_{90}(010)$. Pairs of moments 1, 2 and 3, 4 are strongly coupled via $J_{90}(100)$ but frustration arises because of the intermediate coupling strengths $J_{90}(\frac{1}{2}\ \frac{1}{2}\ \frac{1}{2}) \approx J_{90}(-\frac{1}{2}\ \frac{1}{2}\ \frac{1}{2})$, so that moments 1 and 2 are perpendicular to 3 and 4. The collinear parallel solution is consistent with $J_{90}(100) \approx J_{90}(-\frac{1}{2}\ \frac{1}{2}\ \frac{1}{2}) > J_{90}(\frac{1}{2}\ \frac{1}{2}\ \frac{1}{2})$, $J_{90}(010)$, whereas the antiparallel solution has $J_{90}(100) \approx J_{90}(\frac{1}{2}\ \frac{1}{2}\ \frac{1}{2}) > J_{90}(-\frac{1}{2}\ \frac{1}{2}\ \frac{1}{2})$, $J_{90}(010)$. In both cases, two J_{90} interactions are satisfied while the remaining two are frustrated.

In tetragonal double perovskites, two distinct J_{90} superexchange interactions are expected. However, the disordered octahedral tilts observed for A=Ba (Sec. III A) lower the local symmetry, resulting in $J_{90}(100) \neq J_{90}(010)$ and $J_{90}(\frac{1}{2}\ \frac{1}{2}\ \frac{1}{2}) \neq J_{90}(-\frac{1}{2}\ \frac{1}{2}\ \frac{1}{2})$, as evidenced by the magnetic propagation vector $\mathbf{k}=(\frac{1}{2}\ 0\ \frac{1}{2})$. The A=Ba material adopts a collinear antiparallel magnetic structure and the relative coupling strengths are given above. The magnetic frustration increases significantly compared to A=Ca and Sr, as evidenced by the lowered Neel temperature (10 K) and reduced saturation moment (1.85 μ_B).

Experimentally, the magnetic structure is derived from the magnetic propagation vector and the diffraction intensities. For monoclinic double perovskites, magnetic propagation vectors of $(\frac{1}{2}\ 0\ \frac{1}{2})$ and $(0\ \frac{1}{2}\ \frac{1}{2})$ are found, corresponding to dominant $J_{90}(100)$ or $J_{90}(010)$ interactions, respectively. For the Mn double perovskites in Table IV, the magnetic periodicity along the longer of the a or b cell axes is doubled, and the J_{90} interaction in this direction is dominant, but no such systematic behavior is observed for the Fe or Co double perovskites. From representation analysis, two possible "perpendicular" and two possible "collinear" solutions for the magnetic structure are found, which cannot be distinguished experimentally in most materials because of the small monoclinic angle β. Competition between the $J_{90}(100)$ and $J_{90}(010)$ exchange pathways determines whether $\mathbf{k}=(\frac{1}{2}\ 0\ \frac{1}{2})$ or $\mathrm{k}=(0\ \frac{1}{2}\ \frac{1}{2})$ is adopted, whereas the full basis vector model is determined by the competing $J_{90}(\frac{1}{2}\ \frac{1}{2}\ \frac{1}{2})$ and $J_{90}(-\frac{1}{2}\ \frac{1}{2}\ \frac{1}{2})$ interactions. In higher symmetry cells, the J_{90} exchange interactions become more similar (and eventually identical in cubic symmetry) and the amount of geometric frustration increases, as evidenced by the lowered Neel temperatures and larger frustration factors for the tetragonal and cubic materials in Table IV, for example f=8.5 for cubic Sr_2MnMoO_6.

V. CONCLUSIONS

The crystal and magnetic structures of the (LaA)$CoNbO_6$ (A=Ca, Sr, and Ba) double perovskites have been studied and the importance of geometric magnetic frustration in antiferromagnetic double perovskites is demonstrated. Neutron powder diffraction shows the (LaA)$CoNbO_6$ materials to have an almost fully ordered rocksalt arrangement of Co^{2+} ($3d^7$) and Nb^{5+} ($4d^0$) and to have the $b^-b^-c^+$ (A=Ca, Sr) and $a^0a^0c^-$ (A=Ba) Glazer ordered tilt systems.

All three phases order antiferromagnetically at low temperatures, with a $(\frac{1}{2}\ 0\ \frac{1}{2})$ magnetic propagation vector. For A=Ca and Sr, two "perpendicular" and two "collinear" magnetic structures are possible dependent upon competing 90° exchange interactions between four simple cubic Co-sublattices. These solutions cannot be distinguished experimentally because of the small monoclinic distortion angle ($\beta \approx 89.8^{\circ}$). The tetragonal A=Ba material has a collinear antiparallel magnetic structure.

The Neel temperature *decreases* from 17 K (A=Ca) to 16 K (A=Sr) to 10 K (A=Ba) where an *increase* with average A-site radius is generally expected. This decrease is accompanied by a reduction in the saturation moment from $2.97(2)\mu_B$ (A=Ca) to $2.52(3)\mu_B$ (A=Sr) to $1.85(5)\mu_B$ for A=Ba. These observations are consistent with geometric magnetic frustration in the fcc-Co lattice. This frustration arises from competing 90° exchange interactions between four simple cubic Co sublattices, in which the stronger 180° exchange interactions are fully satisfied. Magnetic frustration is a generally occurring phenomenon in antiferromagnetic double perovskites and increases with cell symmetry as the 90° exchange interactions become more similar.

ACKNOWLEDGMENTS

We thank Dr. E. Suard for help with data collection at ILL, and EPSRC for support to J.-W.G.B. and neutron beamtime.

[1] M.T. Anderson, K.B. Greenwood, G.A. Taylor, and K.R. Poeppelmeier, Prog. Solid State Chem. **22**, 197 (1993).
[2] K.L. Kobayashi, T. Kimura, H. Sawada, K. Terakura, and Y. Tokura, Nature (London) **395**, 677 (1998).
[3] J. Gopalakrishnan, A. Chattopadhyay, S.B. Ogale, T. Venkatesan, R.L. Greene, A.J. Millis, K. Ramesha, B. Hannoyer, and G. Marest, Phys. Rev. B **62**, 9538 (2000).
[4] D.D. Sarma, Curr. Opin. Solid State Mater. Sci. **5**, 261 (2001).
[5] H. van Leuken and R.A. de Groot, Phys. Rev. Lett. **74**, 1171 (1995).
[6] J.W.G. Bos and J.P. Attfield, Phys. Rev. B **69**, 094434 (2004).
[7] J.W.G. Bos and J.P. Attfield, Chem. Mater. **16**, 1822 (2004).
[8] C.R. Wiebe, J.E. Greedan, and G.M. Luke, Phys. Rev. B **65**, 144413 (2002).
[9] C.R. Wiebe, J.E. Greedan, P.P. Kyriakou, G.M. Luke, J.S. Gardner, A. Fukaya, I.M. Gat-Malureanu, P.L. Russo, A.T. Savici, and Y.J. Uemura, Phys. Rev. B **68**, 134410 (2003).
[10] G.J. Blasse, J. Inorg. Nucl. Chem. **27**, 993 (1964).
[11] A.C. Larson and R.B. von Dreele, General Structural Analysis System (GSAS), Report No. LAUR 86-748, Los Alamos National Laboratory, 1994.
[12] A.S. Wills and I.D. Brown, VALIST, CEA, France, 1999.
[13] A.M. Glazer, Acta Crystallogr., Sect. B: Struct. Crystallogr. Cryst. Chem. **B28**, 3384 (1972).
[14] P.M. Woodward, Acta Crystallogr., Sect. B: Struct. Sci. **B53**, 32 (1997).
[15] M.C. Viola, M.J. Martínez-Lope, J.A. Alonso, J.L. Martínez, J.M. De Paoli, S. Pagola, J.C. Pedregosa, M.T. Fernández-Dáaz, and R.E. Carbonio, Chem. Mater. **15**, 1655 (2003).
[16] A.S. Wills, Physica B **276**, 680 (2000).
[17] A. Munoz, J.A. Alonso, M.T. Casais, M.J. Martinez-Lope, and M.T. Fernandez-Diaz, J. Phys.: Condens. Matter **14**, 8817 (2002).
[18] J.E. Greedan, J. Mater. Chem. **11**, 37 (2001).
[19] R. Shannon, Acta Crystallogr., Sect. A: Cryst. Phys., Diffr., Theor. Gen. Crystallogr. **32**, 751 (1972).
[20] J.W.G. Bos and J.P. Attfield, Z. Anorg. Allg. Chem. (unpublished).
[21] J.W.G. Bos and J.P. Attfield (unpublished results).
[22] M.J. Martínez-Lope, J.A. Alonso, and M.T. Casais, Z. Naturforsch [C] **58**, 571 (2003).
[23] A.K. Azad, S.A. Ivanov, S.-G. Eriksson, J. Eriksen, H. Rundlöf, R. Mathieu, and P. Svedlindh, Mater. Res. Bull. **36**, 2215 (2001).
[24] A.K. Azad, S.-G. Eriksson, A. Mellergård, S.A. Ivanov, J. Eriksen, and H. Rundlöf, Mater. Res. Bull. **37**, 1797 (2002).
[25] H. Kawanaka, I. Hase, S. Toyama, and Y. Nishihara, Physica B **281&282**, 518 (2000).